Biosensors and Bioelectronics 282 (2025) 117470

Contents lists available at ScienceDirect

Biosensors and Bioelectronics

journal homepage: www.elsevier.com/locate/bios

Enhanced electrochemiluminescence of mixed-ligand metal-organic framework with suppressed non-radiative transitions for "signal-off" biosensing of β-galactosidase

Mengjiao Li, Chao Wang, Zhiwei Tang, Si Zhang, Guijun Li, Huangxian Ju *

State Key Laboratory of Analytical Chemistry for Life Science, School of Chemistry and Chemical Engineering, Nanjing University, Nanjing, 210023, PR China

ARTICLE INFO

Keywords:
Electrochemiluminescence
Mixed-ligand metal organic framework
Non-radiative transitions
Competition inhibition
Imaging
β-galactosidase

ABSTRACT

Organic molecular emitters usually suffer from the aggregation-caused quenching (ACQ) effect, which significantly decreases their electrochemiluminescence (ECL) efficiency. This work designed a straightforward strategy to alleviate the ACQ effect and thus improve the ECL efficiency by employing a donor-acceptor (D-A) type ligand containing benzothiadiazole group and another ligand with identical connectivity to assemble a mixed-ligand zirconium-based metal organic framework (m-Zr-MOF). Upon the formation of a reticular structure and the distance increase between two ligands, the m-Zr-MOF exhibited alleviating ACQ effect due to the suppressed non-radiative transitions, which was confirmed by the improvements of both quantum yield and fluorescence lifetime. At the molar ratio of **3:1** for two ligands the obtained m-Zr-MOFs displayed the optimal ECL performance, and thus an ECL imaging method was developed for "signal-off" detection of β-galactosidase (β-Gal) by combining its enzymatic property to catalyze the hydrolysis of p-nitrophenyl β-D-galactopyranoside, which generated p-nitrophenol to quench the ECL emission through resonance energy transfer. The proposed method showed a detectable range of 5.0 to 2×10^4 mU/L with a detection limit of 1.92 mU/L, much lower than those of reported fluorescence and electrochemical methods. The designed m-Zr-MOF introduced an innovative concept for the development of mixed-ligand MOFs and their application in ECL imaging.

1. Introduction

Electrochemiluminescence (ECL) is an electrically induced excited light-emitting process, in which the excited states produced by redox reactions return to the ground states (Ding et al., 2002; Miao et al., 2008). ECL has become an essential analytical technique in clinical diagnosis owing to its near-zero background signal and spatiotemporal controllability (Liu et al., 2015). Organic molecular emitters, as an attractive type of organic ECL materials, have shown significant potential in ECL imaging analysis due to their facile versatility in modification and biocompatibility (Wu et al., 2023). However, these emitters exhibit strong molecular spin motion and π-π interactions, leading to aggregation-caused quenching (ACQ) effect (Chen et al., 2018; Guo et al., 2020; Huang et al., 2019) which significantly limits their ECL efficiency and applications. To reduce the ACQ effect and suppress the energy loss, some metal-organic frameworks (MOFs) assembled with these emitters as ligands have been developed to constrain the spin motion of organic molecular emitters (Li et al., 2024; Wang et al., 2023; Zhu et al., 2023). However, the ACQ effect still persists in densely packed and rigid single-ligand MOFs structures (Wu et al., 2021).

Compared to single-ligand MOFs, mixed-ligand MOFs can combine ligands with different functions to realize precise regulation of structure and performance (Pullen et al., 2018). Currently, several methods have been reported to enhance the ECL intensity of MOFs by utilizing redox pairs as mixed ligands to achieve radical accumulation (Jin et al., 2020), co-reactants as ligands to shorten the distance of electron transfer (Zhu et al., 2021) or incorporating short bandgap ligands to facilitate electron transfer (Shao et al., 2023). A strategy to minimalize the ACQ effect of perylene fluorescence has also been proposed by molecular incorporation of isostructural ligands into MOFs to expand the inter-emitter distance and suppress non-radiative transitions (Li et al., 2020). This strategy inspires us to introduce isostructural organic emitters as ligands into MOFs to mitigate the ACQ effect for constructing highly efficient ECL emitters. In view of the merits of donor-acceptor (D-A) ligands, such as intramolecular charge transfer characteristics (Cao et al., 2023b; Xiao et al., 2024), the excellent ECL performance of MOFs constructed with

* Corresponding author.
E-mail address: hxju@nju.edu.cn (H. Ju).

https://doi.org/10.1016/j.bios.2025.117470
Received 4 March 2025; Received in revised form 2 April 2025; Accepted 10 April 2025
Available online 11 April 2025

anthracene-based (Chen et al., 2023) and pyrene-based (Fang et al., 2024) D-A ligands, and the excellent optical characteristics of 4, 4'-(benzo[c][1,2,5]thiadiazole-4,7-diyl) dibenzoic acid (BTDB) with narrow bandgap, good conductivity and semiconductor properties, a π-conjugated D-A ligand containing a strong electron-deficient group, benzothiadiazole (Mallick et al., 2019), this work used BTDB as a D-A ligand for the first time to enhance the charge transfer and designed a mixed-ligand Zr-based MOF (m-Zr-MOF) with low ACQ effect and optimal ECL performance.

The m-Zr-MOF was constructed with 2′,5′-dimethyl-[1,1′:4′,1″-terphenyl]-4,4″-dicarboxylic acid (MTDB) as an isostructural spacer to isolate BTDB ligand (Fig. 1A), and thereby suppress the ACQ effect. MTDB was structurally compatible with BTDB in length and connectivity, and thus could form isoreticular MOF upon their coordination to Zr (IV). Its incorporation increased the instance between BTDB for effectively mitigating the ACQ effect while preserving framework integrity. Moreover, MTDB, featuring methyl-substituted side chains, possesses higher solubility than reported BTDB/triphenylene dicarboxylic acid (Jiang et al., 2022). The ECL emission of designed m-Zr-MOF could be generated from both the excited state BTDB* and the excited state MTDB*, which were produced by the reaction of $BTDB^{\cdot+}$ or $MTDB^{\cdot+}$ radicals with tripropylamine radical (TPrA·), leading to their competition to TPrA·. At a BTDB to MTDB ratio of 3:1, the optimal ECL performance of m-Zr-MOF with over three-fold enhancement in ECL intensity was achieved due to the increased distance between two ligands, suppressed non-radiative transitions and alleviated ACQ effect. As a proof of concept, the m-Zr-MOF was employed for ECL imaging detection of β-galactosidase (β-Gal), a biomarker associated with rare diseases such as aging and primary ovarian cancer (Brunetti-Pierri et al., 2008; Dimri et al., 1995; Sharma et al., 2021), through its catalytic cleavage to the glycosidic bond of p-nitrophenyl β-D-galactopyranoside (PNPG) to produce p-nitrophenol (PNP), which quenched the ECL emission of m-Zr-MOF via resonance energy transfer (RET). The ECL imaging method exhibited high selectivity and sensitivity to β-Gal, demonstrating the excellent application of m-Zr-MOF in ECL analysis.

2. Experimental section

2.1. Materials and reagents

4,4'-(Benzo [c] [1,2,5] thiadiazole-4,7-diyl) dibenzoic acid (BTDB) was purchased from Bide Chemical Co., Ltd. (Shanghai, China). 2′,5′-Dimethyl-[1,1′:4′,1″-terphenyl]-4,4″-dicarboxylicacid (MTDB) was obtained from Meryer Chemical Technology Co., Ltd. (Shanghai, China). Zirconium tetrachloride ($ZrCl_4$) was provided by Macklin Biochemical Co., Ltd. (Shanghai, China). N, N-Dimethylformamide (DMF), methanol (CH_3OH), dimethyl sulfoxide-d_6 (DMSO-d_6), sodium phosphate dibasic dodecahydrate ($Na_2HPO_4{\cdot}12H_2O$), potassium dihydrogen phosphate (KH_2PO_4), concentrated hydrochloric acid (HCl) and acetic acid (HAc) were obtained from Nanjing Chemical Reagent Co., Ltd. (Nanjing, China). Tripropylamine (TPrA, >98 %) was purchased from J&K Chemical Ltd. (Beijing, China). Indium tin oxide (ITO) glass slides (100 mm × 100 mm × 1.1 mm) were purchased from Zhuhai Kaivo Optoelectronic Technology Co., Ltd. (Zhuhai, China). β-Galactosidase (β-Gal) was provided by Yuanye Bio-Technology Co., Ltd. (Shanghai, China). 4-Nitrophenyl-β-D-galactopyranoside (PNPG) was purchased from Shanghai Haohong Bio-pharmaceutical Technology Co., Ltd. (Shanghai, China). Catalase, lysozyme, and glucose oxidase were obtained from Macklin Biochemical Co., Ltd. (Shanghai, China). Phosphate buffer saline (PBS, 0.1 M, pH 7.4) was prepared by mixing the stock solutions of KH_2PO_4 and Na_2HPO_4. All aqueous solutions were prepared with ultrapure water (Milli-Q, Millipore).

2.2. Apparatus

Solid-state ultraviolet–visible diffuse reflectance spectra (UV–Vis DRS) were recorded on a Shimadzu UV-3600 spectrophotometer. Powder X-ray diffraction (PXRD) patterns were collected on a Bruker D8-Advance diffractometer at 40 kV, 40 mA. Fluorescence (FL) spectra and lifetimes were measured on a FLS-980 fluorescence spectrophotometer (Edinburgh, U.K.). Absolute FL quantum yields were measured

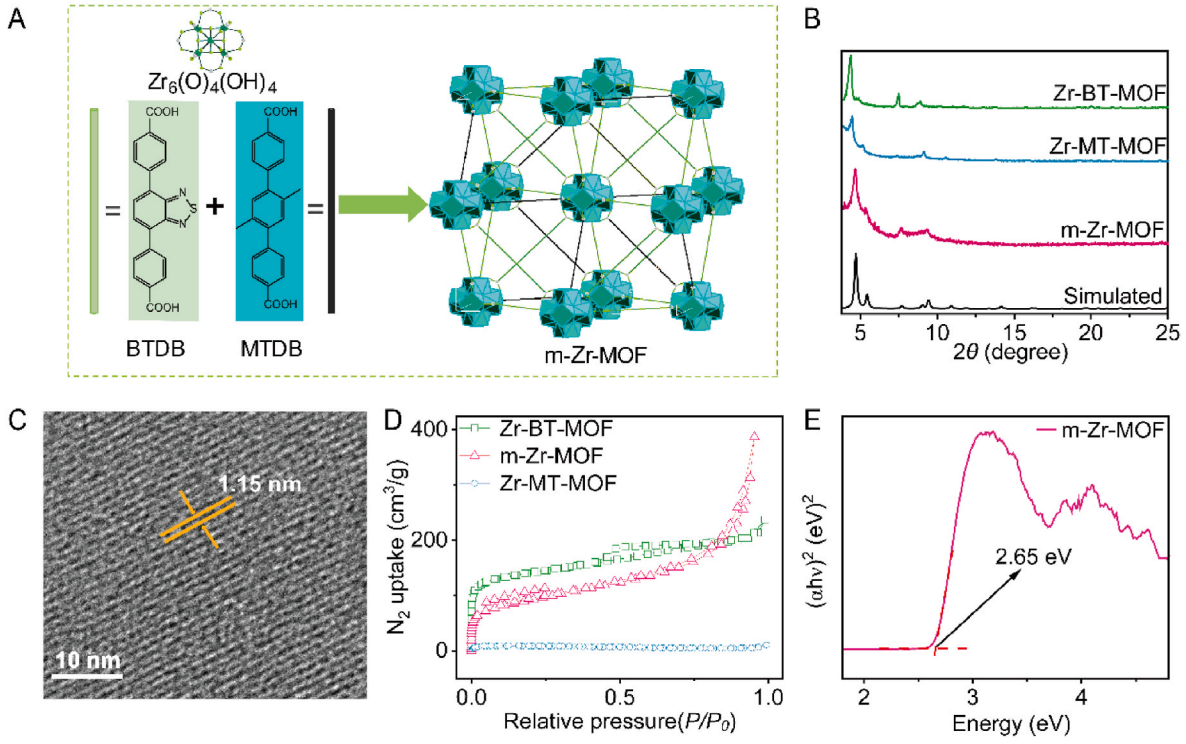

Fig. 1. (A) Schematic diagram of m-Zr-MOF synthesis. (B) PXRD patterns of m-Zr-MOF, Zr-MT-MOF, Zr-BT-MOF and simulated UiO-68. (C) HRTEM image of m-Zr-MOF. (D) N_2 adsorption-desorption isotherms of m-Zr-MOF, Zr-MT-MOF and Zr-BT-MOF. (E) Tauc plot of m-Zr-MOF.

on a FLS-980 fluorescence spectrophotometer (Edinburgh, U.K.) combined with an integrating sphere. Scanning electron microscopic (SEM) images were obtained using a JEOL JSM-7800F. High-resolution transmission electron microscopic (HRTEM) image was collected on a Talos F200X high-resolution transmission electron microscope (FEI, American). Thermal stability analyses were performed on a thermogravimetric (TG) instrument (Netzchen, STA449F3) in 25–800 °C under a nitrogen atmosphere with a flow rate of 16 mL/min and a heating rate of 10 °C/min, and the sample mass was about 10 mg. The nuclear magnetic resonance spectrum (NMR) was measured with Bruker AvanceIII 500HD spectrometer (Germany) at 400 MHz using deuterated DMSO-d_6 as solvent and tetramethylsilane (TMS) as an internal reference. X-ray photoelectron spectroscopic (XPS) analyses were performed on a PHI5000 X-ray photoelectron spectrometer (Ulvac-Phi, Japan). Voltammetric experiments were performed using a CHI 630D electrochemical workstation (Chenhua Shanghai, China). ECL measurements were performed on a MPI-EII ECL analyzer (Xi'an Remex, China) with a photomultiplier tube (PMT). The voltage of PMT was set at 600 V for anodic ECL. The ECL imaging system was equipped with a focus len (EF 50 mm f/1.2 L USM, Canon), an electron multiplying charge coupled device (EMCCD, iXon Ultra, Andor, UK), and a CHI-660D electrochemical workstation along with a three-electrode system containing a modified Au/ITO as working electrode, a platinum wire as counter electrode, and a Ag/AgCl electrode wire as reference electrode. ECL images were recorded by scanning between 0 and +1.5 V at 0.1 V/s in 0.1 M PBS (pH 7.4) containing 75 mM TPrA and analyzed by ImageJ software.

2.3. Preparation of Zr-BT-MOF, Zr-MT-MOF and m-Zr-MOFs

Single-ligand Zr-BT-MOF and Zr-MT-MOF were respectively synthesized with BTDB and MTDB according to previous reports with minor modifications (Zhang et al., 2016). Specifically, a 250 mL round-bottom flask containing $ZrCl_4$ (0.33 mmol, 77.22 mg), BTDB (0.26 mmol, 97.76 mg) or MTDB (0.26 mmol, 90.05 mg), DMF (75 mL) and HAc (6 mL) was heated in an oil bath pan at 100 °C for 48 h. After cooling to room temperature, the product was separated by centrifugation and washed with DMF and CH_3OH for three times, respectively. Finally, the product was dried under vacuum at 60 °C. Following this synthetic approach, a series of m-Zr-MOFs were successfully obtained at different molar ratios of BTDB to MTDB with a total amount of 0.26 mmol, as detailed in Table S1.

To analyze the molar ratio of BTDB to MTDB in m-Zr-MOFs, 10 mg of obtained products was digested with 300 μL of concentrated HCl, dried in an oven at 80 °C, and dispersed in 600 μL of DMSO-d_6 to perform nuclear magnetic resonance (NMR) spectrometric measurements.

2.4. Preparation of Au/ITO and ECL imaging array

ITO glass was cleaned with toluene, acetone, ethanol and ultrapure water for 20 min each, followed by drying with nitrogen gas. It was then evaporatively deposited with 5 nm Cr and 50 nm Au to obtain Au/ITO glass. The Au/ITO glass was finally pasted with a porous sticker to form the 4 × 7 wells (diameter 2 mm, depth 1 mm) for ECL detection.

2.5. ECL imaging detection

After the mixtures of 4.94 mL of phosphate buffer saline (PBS pH 7.4), 50 μL of 100 mM PNPG, and 10 μL of β-Gal solution at different concentrations were incubated at 37 °C for 40 min, and then heated in a water bath at 90 °C for 10 min to inactivate β-Gal, 2 μL of the mixture and 3 μL of m-Zr-MOF dispersion (0.75 mg/mL) were added to each well of the array to volatilize at 37 °C for 45 min. Afterward, 1.5 mL of 0.1 M PBS (pH 7.4) containing 75 mM TPrA was added in each well to perform the ECL imaging.

3. Results and discussion

3.1. Characterization of Zr-BT-MOF, Zr-MT-MOF and m-Zr-MOF

The powder X-ray diffraction (PXRD) patterns of Zr-BT-MOF, Zr-MT-MOF and m-Zr-MOF were consistent with the pattern of simulated UiO-68 (Fig. 1B), confirming the successful construction of these materials with the same topology as UiO-68. High-resolution transmission electron microscopic (HRTEM) image of m-Zr-MOF showed distinct lattice fringes with a distance of 1.15 nm (Fig. 1C), corresponding to (022) crystal facet. Both m-Zr-MOF and Zr-BT-MOF were mainly composed of sheets (Figs. S1 and S2), while Zr-MT-MOF displayed a block-like structure (Fig. S3). Energy-dispersive X-ray spectroscopy (EDS) proved the uniform distribution of C, O, N, S and Zr elements in both m-Zr-MOF and Zr-BT-MOF (Figs. S1 and S2) and the presence of C, O and Zr elements in Zr-MT-MOF (Fig. S3), in agreement with X-ray photoelectron spectroscopic (XPS) results (Figs. S4–S6). In the O 1s XPS spectra of m-Zr-MOF, Zr-BT-MOF and Zr-MT-MOF, Zr-O bonds were observed (Figs. S4B–S6B), suggesting successful coordination of the ligand with Zr, which led to the observations of C-C C-O, C-C=O, C=N, and/or N-S in the ligands. Additionally, the Zr 3d XPS spectra displayed two distinct peaks assigned to Zr $3d_{5/2}$ and Zr $3d_{3/2}$ (Fig. S4E, S5E and S6C), identifying the presence of Zr in these materials. Moreover, the Brunauer-Emmett-Teller (BET) surface areas of m-Zr-MOF, Zr-BT-MOF and Zr-MT-MOF were measured from isothermal nitrogen adsorption-desorption curves (Fig. 1D) to be 354.13, 448.39 and 25.70 m^2/g, respectively. The average pore sizes of Zr-BT-MOF and Zr-MT-MOF obtained by the BJH model were 3.7 nm (Fig. S7A) and 26.1 nm (Fig. S7B), respectively, indicating the mesoporous structures. Notably, m-Zr-MOF integrated the characteristics of both Zr-BT-MOF and Zr-MT-MOF, as evidenced by the presence of two pore sizes within its structure (Fig. S7C). Compared to Zr-BT-MOF and m-Zr-MOF, the smaller BET surface area of Zr-MT-MOF could be attributed to smaller ligand spatial resistance and larger pore size (Masika et al., 2012). The m-Zr-MOF with the high surface area and large pores could facilitate the transportation of radicals, and co-reactant in MOFs (Yang et al., 2024).

Thermogravimetric analyses of m-Zr-MOF, Zr-BT-MOF and Zr-MT-MOF demonstrated their stable structures up to 500 °C in nitrogen atmosphere (Fig. S8). The UV–vis absorption spectrum of Zr-BT-MOF showed two absorption peaks at 300 nm and 390 nm, originated from the large conjugated structure of BTDB, while Zr-MT-MOF exhibited a narrow absorption peak at 200 nm, consistent with the characteristics of MTDB (Fig. S9). The absorption bands of m-Zr-MOF at 200 nm, 300 nm and 390 nm (Fig. S9) further demonstrated the presence of two ligands in the framework. The band gaps of Zr-BT-MOF and Zr-MT-MOF were determined by Tauc plots to be 2.65 and 3.68 eV (Figs. S10A and S10B), similar to those of BTDB and MTDB (Figs. S10C and S10D), respectively. The band gap of m-Zr-MOF was measured to be 2.65 eV (Fig. 1E), inherited from Zr-BT-MOF due to the higher amount of BTDB. These results demonstrate the semiconductor properties of three kinds of MOFs.

3.2. ECL and FL behaviors of m-Zr-MOF, Zr-BT-MOF and Zr-MT-MOF

The ECL properties of m-Zr-MOF, Zr-BT-MOF and Zr-MT-MOF were investigated by using TPrA as an anodic co-reactant. The onset oxidation potential of m-Zr-MOF was observed at +0.6 V, which was close to that of Zr-BT-MOF, and lower than that of +0.75 V for Zr-MT-MOF and/or co-reactant TPrA (Fig. 2A and S11), which was ascribed to the presence of more BTDB in m-Zr-MOF. In the presence of 10 mM TPrA, the ECL emission peaks of both m-Zr-MOF and Zr-BT-MOF appeared at +1.1 V, while the ECL peak of Zr-MT-MOF occurred at +1.3 V (Fig. 2B), close to the ECL emission peaks of BTDB and MTDB, respectively (Fig. S12). Compared with BTDB and MTDB, both Zr-BT-MOF and Zr-MT-MOF exhibited an enhancement in ECL intensity, and m-Zr-MOF showed much stronger ECL emission (Figs. S11 and 2B). The ECL enhancement

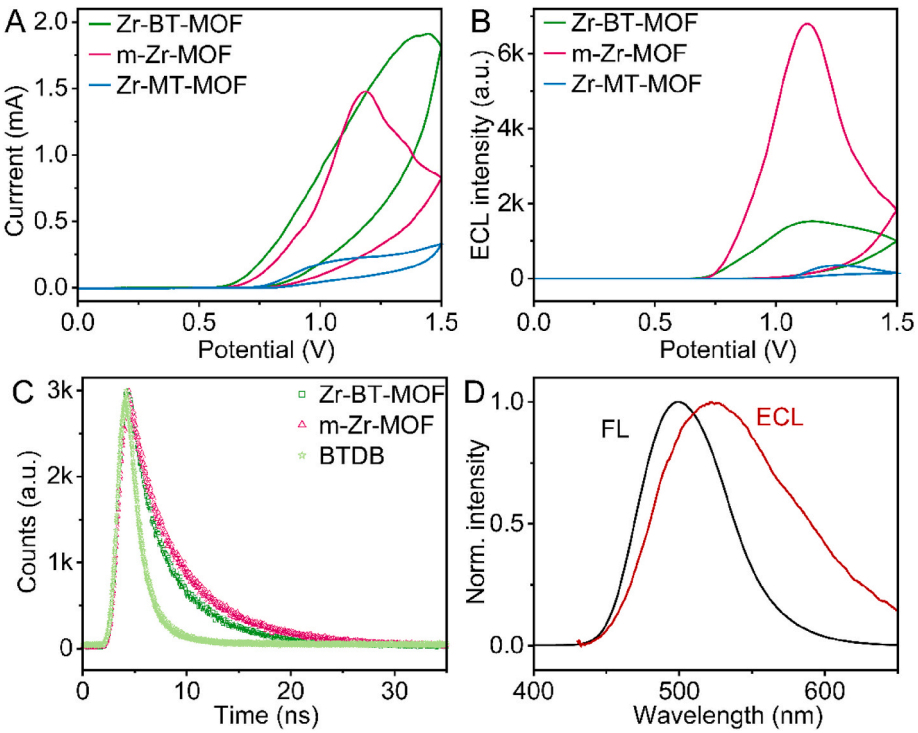

Fig. 2. (A) CV and (B) ECL curves of m-Zr-MOF, Zr-MT-MOF and Zr-BT-MOF modified GCEs in 0.1 M pH 7.4 PBS with 10 mM TPrA. (C) Fluorescence lifetime decay curves of BTDB, Zr-BT-MOF and m-Zr-MOF. (D) ECL and PL spectra of m-Zr-MOF.

of Zr-BT-MOF and Zr-MT-MOF could be attributed to the effective anchoring of the ligands within the framework, which restricted their rotational and vibrational motions and thereby reduced non-radiative energy loss (Li et al., 2022; Wang et al., 2024). The higher ECL intensity and the lower ECL potential of Zr-BT-MOF in comparison with Zr-MT-MOF was partially ascribed to the D-A type ligand and the conjugated structure of the BTDB ligand, which facilitated intramolecular electron transfer (Luo et al., 2021). In addition, the lamellar structure and larger specific surface area of Zr-BT-MOF also contributed to achieving higher ECL intensity. The maximum ECL intensity of m-Zr-MOF, which was more than three times higher than that of Zr-BT-MOF (Fig. 2B), resulted from the suppressed non-radiative transitions and alleviated ACQ effect, as described below.

The suppression of non-radiative transitions and ACQ effect on ECL emission of m-Zr-MOF was investigate with fluorescence (FL) and ECL experiments. The FL peak of BTDB was located at 500 nm, while the FL peaks of Zr-BT-MOF and m-Zr-MOF exhibited a sequential blue shift towards higher energy states due to the gradual weakening of π-π stacking interactions in BTDB (Fig. S13A), which also resulted in the shift of ECL emissions of both Zr-BT-MOF and m-Zr-MOF (Fig. S13B) (Wong et al., 2020). The similar ECL spectra of Zr-BT-MOF and m-Zr-MOF to that of BTDB indicated that the ECL peak of Zr-BT-MOF and m-Zr-MOF originated from BTDB. From the FL spectra, the quantum yield of m-Zr-MOF was measured to be 21.95 %, higher than those of Zr-BT-MOF (19.85 %) and BTDB (3 %). The sequential increase was attributed to ligand fixation in the MOF and the increasing distance between BTDB due to the addition of the MTDB ligand (Jiang et al., 2022). In addition, the FL lifetimes of BTDB, Zr-BT-MOF and m-Zr-MOF were measured to be 2.01, 4.65 and 5.79 ns, respectively (Fig. 2C–Table S2). The longer FL lifetime and higher quantum yield of m-Zr-MOF suggested that the reticular structure and the incorporation of additional ligands could effectively reduce the non-radiative transitions of the excited states and prevent the ACQ effect (Cao et al., 2023a; Song et al., 2024). Compared to the FL emission the ECL spectrum of m-Zr-MOF displayed a red shift of 20 nm (Fig. 2D), suggesting that the ECL emission of m-Zr-MOF was generated through surface-state exciton transitions rather than bandgap transitions (Wu et al., 2014). Meanwhile, the ECL efficiency of m-Zr-MOF was measured to be 6.77 % vs. 1 mM $[Ru(bpy)_3]^{2+}$/TPrA, which was higher than other mixed-ligand MOFs (Table S3), indicating the prevented ACQ effect. Under optimal reaction and measurement conditions, the m-Zr-MOF modified electrodes prepared in different batches showed a relative standard deviation (RSD) of 1.55 % in ECL intensity (Fig. S14), suggesting a good reproducibility of m-Zr-MOF properties.

3.3. Characterization of m-Zr-MOFs with different ratios of ligands

To further investigate the detailed ECL mechanism of m-Zr-MOF, the m-Zr-MOFs with BTDB to MTDB molar ratios of 3:1, 1:1 and 1:3, denoted as m-Zr-MOF (**3:1**), (**1:1**) and (**1:3**), were synthesized and proved by PXRD patterns, respectively (Fig. 3A). The NMR spectrometric measurements demonstrated that the proportions of the two ligands were very close to the ratios used for synthesis (Figs. S15–S17). The UV–vis absorption spectra of all three m-Zr-MOFs (Fig. 3B) exhibited the characteristic absorption peaks corresponding to BTDB and MTDB. In addition, the increasing proportion of MTDB led to red shift of the absorption peak, indicating the increased contribution of MTDB ligand. In contrast to the sheet-like structure of m-Zr-MOF (**3:1**) (Fig. S1), both m-Zr-MOF (**1:1**) and (**1:3**) displayed block-like morphologies (Figs. S18 and S19), which were similar to Zr-MT-MOF. The BET surface areas (Fig. 3C) of m-Zr-MOF (**3:1**), (**1:1**) and (**1:3**) were measured to be 354.13, 34.41 and 2.87 m^2/g, respectively. The morphology and structure of m-Zr-MOF (**3:1**) were similar to those of Zr-BT-MOF, while the morphology and structure of m-Zr-MOF (**1:1**) and (**1:3**) were similar to those of Zr-MT-MOF.

With the increasing proportion of MTDB, the FL peaks of m-Zr-MOFs (Fig. 3D) also exhibited a slight blue shift derived from the weakening of π-π stacking interactions, but their initial oxidation peaks remained consistent (Fig. 4A). At high proportion of MTDB, the ECL-potential showed two distinct emission peaks at +1.1 and 1.35 V, denoted as ECL I and ECL II, respectively (Fig. 4B). The potential of ECL I closely matched the ECL peak potential of m-Zr-MOF (**3:1**), Zr-BT-MOF and

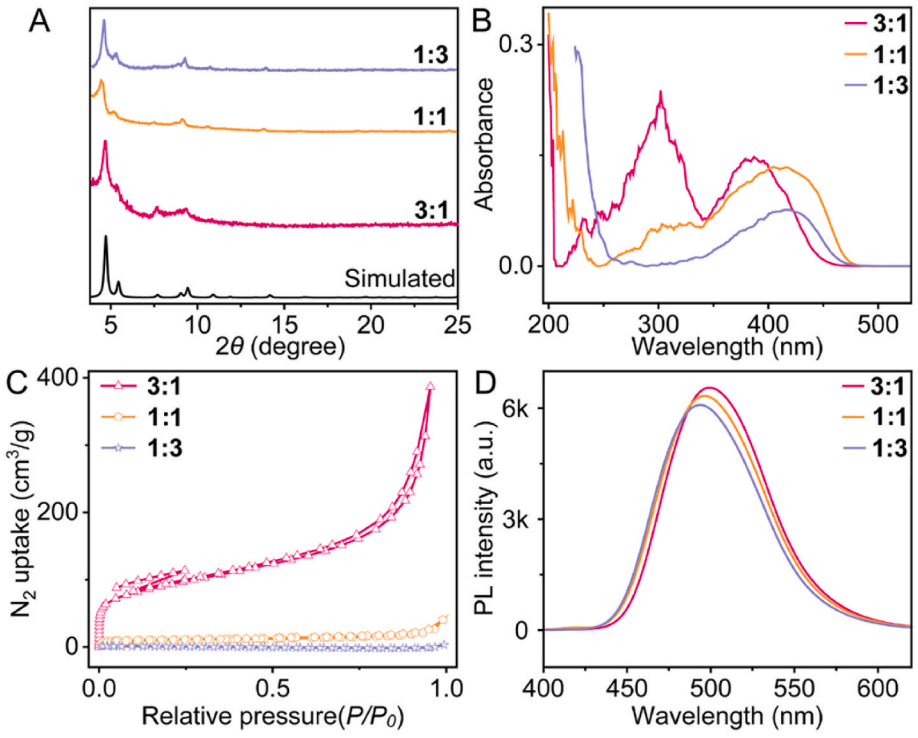

Fig. 3. (A) PXRD patterns, (B) UV–vis spectra, (C) nitrogen adsorption-desorption isotherms and (D) FL spectra of m-Zr-MOF (**3:1**), (**1:1**) and (**1:3**).

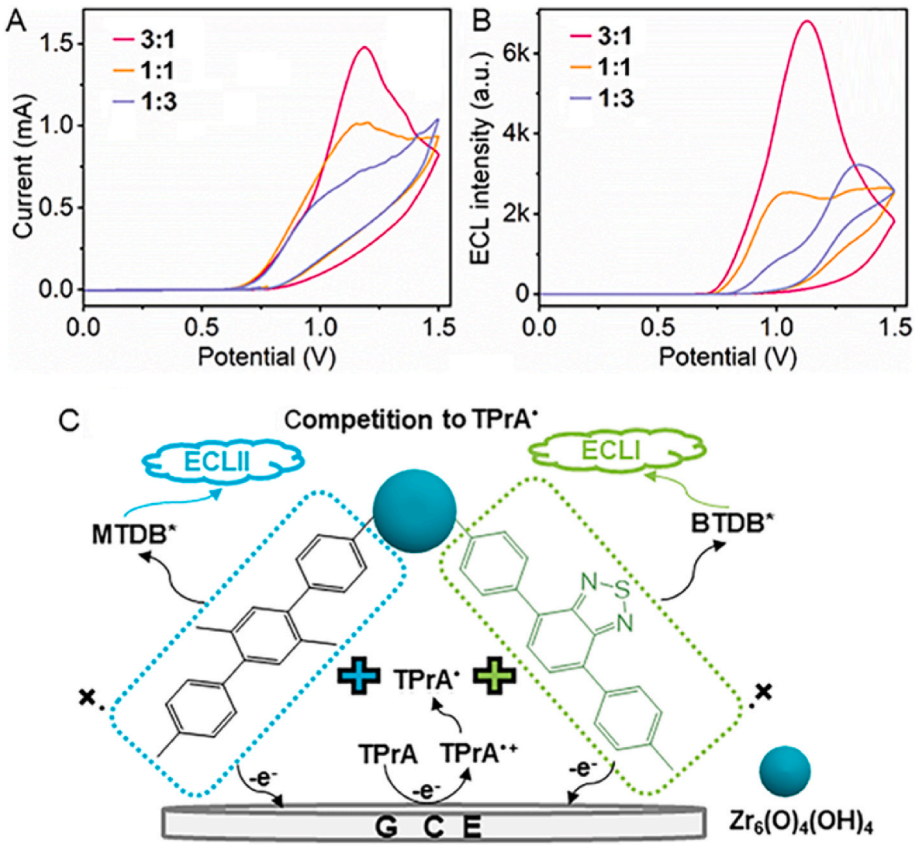

Fig. 4. (A) CV and (B) ECL curves of m-Zr-MOF (**3:1**), (**1:1**) and (**1:3**) modified GCEs in 0.1 M PBS containing 10 mM TPrA. (C) Mechanism of ECL I and ECL II generated by m-Zr-MOF.

BTDB (Fig. 4B and S12), indicating the same excited state species, BTDB* produced from the reaction of $TPrA^{\cdot}$ with oxidized BTDB, $BTDB^{\cdot+}$. ECL II occurred at a potential close to those of both MTDB and Zr-MT-MOF (Fig. S11A), suggested that it was derived from the excited MTDB ligand. Thus upon the potential scanning, two oxidized ligands competitively reacted with produced $TPrA^{\cdot}$ radical to form corresponding excited state species (Fig. 4C), which led to the intensity change of two ECL emissions with the varied ratio of BTDB to MTDB. Interestingly, m-Zr-MOF (**3:1**) showed the strongest ECL emission (Fig. 4B and Fig. S11B), but its FL quantum yield was lowest, compared to 47.08 % and 64.86 % of m-Zr-MOF (**1:1**) and (**1:3**), which could be attributed to the further distance between BTDB at high proportion of MTDB. The low ECL emission of m-Zr-MOF (**1:1**) and (**1:3**) resulted from their smaller specific surface areas and the competition of oxidized MTDB with oxidized BTDB to react with produced $TPrA^{\cdot}$ radical. The former was unfavorable for contact with co-reactant. Therefore, incorporating moderate MTDB to synthesize m-Zr-MOF could increase the distance between the ligands, thus realizing the ECL intensity improvement.

3.4. ECL detection of β-gal

Using m-Zr-MOF (**3:1**) as an emitter, which exhibited good stability of ECL emission over two weeks (Fig. S20), an ECL imaging method was designed for the detection of β-Gal. The array of ECL detection wells was prepared by pasting a porous sticker on conductive Au/ITO, which acted as a substrate for easier oxidation of TPrA on Au (Wang et al., 2018; Pan et al., 2015). After PNPG was catalytically hydrolyzed by β-Gal to produce PNP, the product was added in the well containing m-Zr-MOF (**3:1**) to perform ECL imaging in 0.1M pH 7.4 PBS with 75 mM TPrA (Fig. 5A). The detection principle was firstly demonstrated by the overlapped FL emission of m-Zr-MOF with the absorption band of PNP (Fig. 5B), which led to the quenching of the excited BTDB species in m-Zr-MOF by PNP via a RET process. The quenching resulted from the interaction between Lewis base N-atoms in BTDB ligand and H-atoms in the hydroxyl group of PNP to form hydrogen bond (Fig. 5C) (Sk et al., 2016; Song et al., 2014), which shortened donor-acceptor distance and thus facilitated the RET process from excited BTDB species to PNP. The concentrations of m-Zr-MOF and co-reactant were optimized to be 0.75 mg/mL (Fig. S21A) and 75 mM (Fig. S21B), respectively. Additionally, the concentration of PNPG and reaction time for β-Gal catalytic hydrolysis were also optimized to be 1.0 mM and 40 min, respectively (Figs. S21C and S21D).

Under optimal conditions, the ECL images became progressively darker as the concentration of β-Gal increased from 5.0 to 2×10^4 mU/L, which showed a good linear relationship with the logarithm of β-Gal

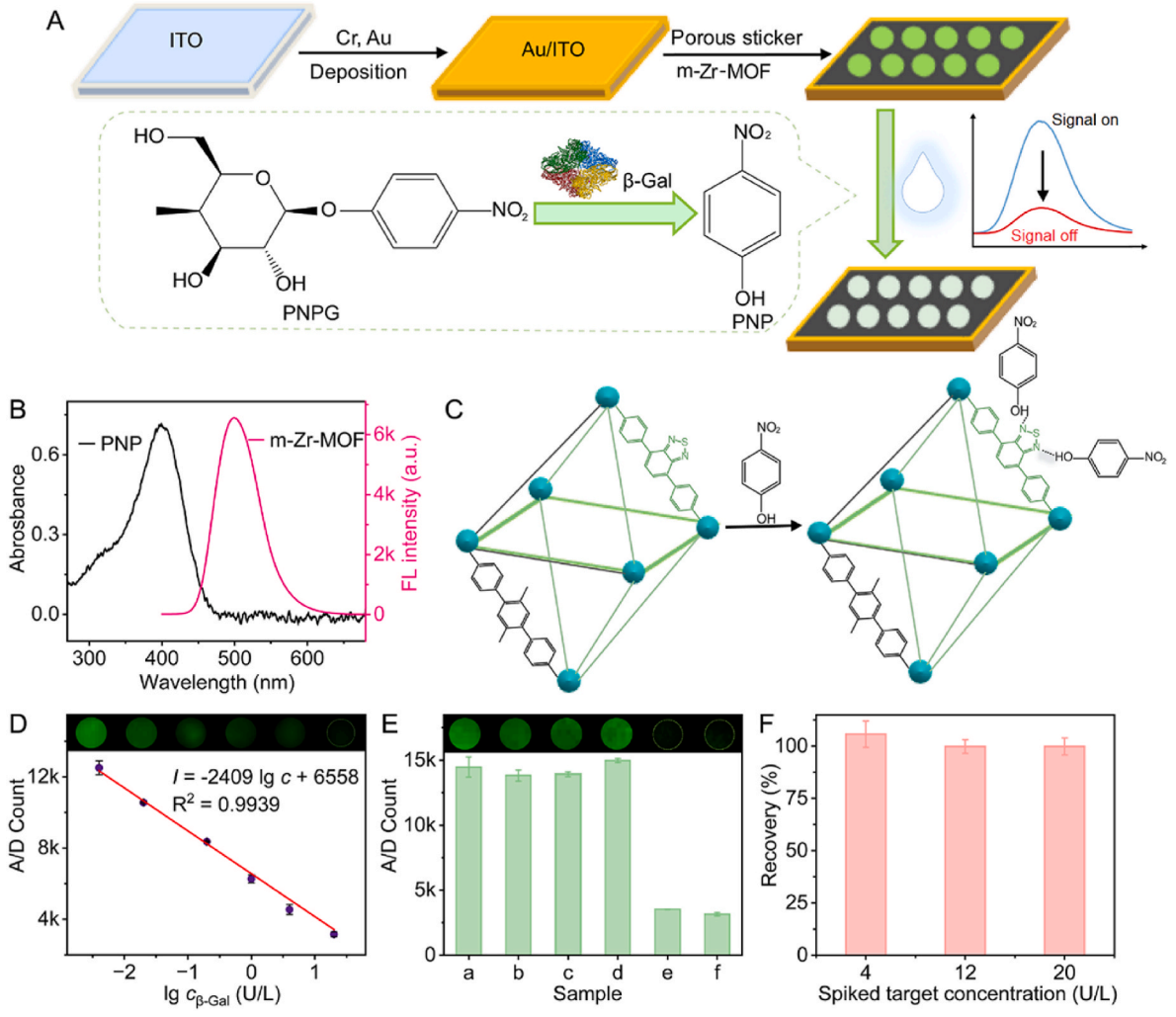

Fig. 5. (A) Diagram of ECL imaging for β-Gal detection at m-Zr-MOF/ITO array. (B) Absorption spectrum of PNP and FL spectrum of m-Zr-MOF. (C) Schematic diagram of Interaction of the N sites of m-Zr-MOF with the hydroxyl group of PNP. (D) ECL images at different β-Gal concentrations and plot of ECL intensity vs β-Gal concentration. (E) Selectivity of the ECL imaging strategy for β-Gal. 200 U/L catalase (a), lysozyme (b), glucose oxidase (c), the mixture of (a)–(c) (d), 20 U/L β-Gal (e) and the mixture of (d) and (e) (f). (F) Recovery at different β-Gal concentrations in 100-fold diluted human serum samples ($n = 3$).

Table 1
Comparison of this method with previously reported approaches for β-Gal detection.

Methods	Materials	Linear range (mU/L)	LOD (mU/L)	Refs
Fluorescence	N-CQDs	50–3000	23	Wang et al. (2022)
Fluorescence	DMC-β-gal	0–1.2 × 10^4	298	Li et al. (2022)
Fluorescence	Carbon dots	1900–7 × 10^4	600	Tang et al. (2017)
Fluorescence	TMG based probe	0–5 × 10^4	560	Zhang et al. (2019)
Fluorescence	Au-Pt NCs	2500–2.5 × 10^4	1200	Sun et al. (2023)
Fluorescence	GQDs	20–2 × 10^4	4400	Xie et al. (2020)
Electrochemistry	Pygal	1500–3 × 10^5	100	Dong et al. (2022)
ECL	m-Zr-MOF	5–2 × 10^4	1.92	This work

concentration (Fig. 5D). The linear equation was $I = -2409 \lg c_{\beta\text{-Gal}} + 6558$ with a correlation coefficient of 0.9939, and the limit of detection (LOD) calculated by the 3σ method was 1.92 mU/L, which was lower than those of reported fluorescence and electrochemical methods (Table 1). The selectivity of the detection method was evaluated using 200 U/L catalase, lysozyme, and glucose oxidase as potential interferents, and they hardly affected the ECL signals of m-Zr-MOF (Fig. 5E). Moreover, their mixture with β-Gal also showed the signal identical to that of β-Gal alone, demonstrating the good specificity. Recovery experiments were further carried out by spiking β-Gal in 100-fold diluted human serum sample. The recoveries of β-Gal were found in the range from 99 % to 106 % (Fig. 5F), indicating excellent accuracy and reliability of the proposed method in practical applications.

4. Conclusion

A simple strategy for enhancing the ECL efficiency of MOFs has been designed by using D-A-type BTDB and an isostructural spacer MTDB to construct m-Zr-MOF. The mixed-ligand MOF shows reduced ACQ effect and suppressed non-radiative transitions of the excited states due to the increased distance between BTDB ligands, leading to a FL quantum yield of 21.95 %, slightly longer FL lifetime and excellent ECL efficiency. Both the BET surface areas and the pore size of m-Zr-MOF are suitable to facilitate the transportation of radicals and co-reactant in MOFs, leading to more than three-fold enhanced ECL emission of m-Zr-MOF (**3:1**). An ECL imaging method has also been proposed with m-Zr-MOF (**3:1**) to detect β-Gal, which shows low detection limit and good specificity, demonstrating the promising application of designed m-Zr-MOF and proposed ECL imaging method, such as the detection of alkaline phosphatase, β-glucosidase, multiple antigens and miRNA based on the similar principle and the enhanced ECL performance. In addition, the proposed m-Zr-MOF can also be used to develop smartphone-based portable ECL devices for point-of-care detection.

CRediT authorship contribution statement

Mengjiao Li: Writing – original draft, Data curation, Conceptualization. **Chao Wang:** Writing – original draft, Methodology. **Zhiwei Tang:** Writing – original draft, Methodology. **Si Zhang:** Validation. **Guijun Li:** Software, Methodology, Conceptualization. **Huangxian Ju:** Writing – review & editing, Methodology, Funding acquisition, Conceptualization.

Notes

The authors declare no competing financial interest.

Data availability

Data will be made available on request.

Declaration of competing interest

The authors declare that there is no conflict of interest.

Acknowledgements

This work was financially supported by the National Natural Science Foundation of China (21827812, 21890741).

Appendix A. Supplementary data

Supplementary data to this article can be found online at https://doi.org/10.1016/j.bios.2025.117470.

References

Brunetti-Pierri, N., Scaglia, F., 2008. Genet. Metab 94 (4), 391–396.
Cao, W.W., Yuan, R., Wang, H.J., 2023a. Anal. Chem. 95, 7640–7647.
Cao, W.W., Zhu, X., Li, Q., Yuan, R., Wang, H.J., 2023b. Chem. Eng. J. 475, 146225.
Chen, G.X., Wang, X.Y., Dai, W.J., Liang, L., Luo, Z.L., Chen, C.R., Zhen, S.J., Huang, C.Z., Li, Y.F., 2023. Anal. Chem. 95 (17), 7030–7035.
Chen, Y.X., Min, X.H., Zhang, X.Q., Zhang, F.L., Lu, S.M., Xu, L.P., Lou, X.D., Xia, F., Zhang, X.J., Wang, S.T., 2018. Biosens. Bioelectron. 111, 124–130.
Ding, Z., Quinn, B.M., Haram, S.K., Pell, L.E., Korgel, B.A., Bard, A.J., 2002. Science 296, 1293–1297.
Dimri, G.P., Lee, X., Basile, G., Acosta, M., Scott, G., Roskelley, C., Medrano, E.E., Linskens, M., Rubelj, I., Pereira-Smith, O., 1995. Natl. Acad. Sci. USA. 92, 9363–9367.
Dong, H., Zhao, L., Zhu, X., Wei, X.H., Zhu, M.H., Ji, Q.M., Luo, X.K., Zhang, Y.T., Zhou, Y., Xu, M.T., 2022. Biosens. Bioelectron. 210, 114301.
Fang, J., Dai, L., Feng, R., Cao, W., Ren, X., Li, X., Wu, D., Wei, Q., Ma, H., 2024. J. Colloid Interface Sci. 665, 934–943.
Guo, M.C., Song, H., Li, K., Ma, M.C., Liu, Y., Fu, Q., He, Z.G., 2020. Med. Res. Rev. 40, 27–53.
Huang, Y.J., Wang, Z.R., Chen, Z., Zhang, Q.C., 2019. Angew. Chem. Int. Ed. 58, 9696–9711.
Jiang, Z.W., Zheng, H.Q., Guan, L.L., Yang, Y., Cui, Y.J., Qian, G.D., 2022. J. Mater. Chem. C 10, 10473–10479.
Jin, Z.C., Zhu, X.R., Wang, N.N., Li, Y.F., Ju, H.X., Lei, J.P., 2020. Angew. Chem. Int. Ed. 59, 10446–10450.
Li, H.Y., Shao, M.Y., Fang, J.L., Li, Y.Y., Sun, X.J., Ren, X., Wei, Q., Ju, H.X., Ma, H.M., 2024. Chem. Eng. J. 495, 153315.
Li, J.L., Yuan, S., Qin, J.S., Huang, L., Bose, R., Pang, J.D., Zhang, P., Xiao, Z., Tan, K., Malko, A.V., Cagin, T., Zhou, H.C., 2020. ACS Appl. Mater. Interfaces 12 (23), 26727–26732.
Li, J.S., Jia, H.Y., Ren, X., Li, Y.Y., Liu, L., Feng, R.Q., Ma, H.M., Wei, Q., 2022. Small 18, 2106567.
Li, Y., Liu, F.Y., Zhu, D.R., Zhu, T.Y., Zhang, Y.X., Li, Y.L., Luo, J.G., Kong, L.Y., 2022. Talanta 237, 122952.
Liu, Z.Y., Qi, W.J., Xu, G.B., 2015. Chem. Soc. Rev. 44, 3117–3142.
Luo, R.G., Lv, H.F., Liao, Q.B., Wang, N.N., Yang, J.R., Li, Y., Xi, K., Wu, X.J., Ju, H.X., Lei, J.P., 2021. Nat. Commun. 12, 6808.
Mallick, A., El-Zohry, A.M., Shekhah, O., Yin, J., Jia, J., Aggarwal, H., Emwas, A.H., Mohammed, O.F., Eddaoudi, M., 2019. J. Am. Chem. Soc. 141, 7245–7249.
Masika, E., Mokaya, R., 2012. J. Phys. Chem. C 116 (49), 25734–25740.
Miao, W., 2008. Chem. Rev. 108, 2506–2553.
Pan, S.L., Liu, J., Hill, C.M., 2015. J. Phys. Chem. C 119 (48), 27095–27103.
Pullen, S., Clever, G.H., 2018. Acc. Chem. Res. 51 (12), 3052–3064.
Shao, M.Z., Sun, Y.Z., Li, Y.Y., Wu, Z.H., Li, X.Y., Zhang, R.Z., Zhang, L.B., 2023. Biosens. Bioelectron. 237, 115530.
Sharma, S.K., Poudel Sharma, S., Leblanc, R.M., 2021. Enzyme Microb. Technol. 150, 109885.
Sk, M., Biswas, S., 2016. CrystEngComm 18, 3104–3113.
Song, L.L., Gao, W.Q., Jiang, S., Yang, Y.C., Chu, W.Q., Cao, X.T., Sun, B., Cui, L., Zhang, C.Y., 2024. Nano Lett. 24, 6312–6319.
Song, X.Z., Song, S.Y., Zhao, S.N., Hao, Z.M., Zhu, M., Meng, X., Wu, L.L., Zhang, H.J., 2014. Adv. Funct. Mater. 24, 4034–4041.
Sun, H., Lv, Y., Zhang, J., Zhou, C., Su, X., 2023. Anal. Chim. Acta 1252, 341010.
Tang, C., Zhou, J., Qian, Z.S., Ma, Y.Y., Huang, Y.Y., Feng, H., 2017. J. Mater. Chem. B 5, 1971–1979.
Wang, J.W., Du, Y., Du, J.X., 2022. Microchim. Acta 189, 282.
Wang, N.N., Feng, Y.Q., Wang, Y.F., Ju, H.X., Feng, Y., 2018. Anal. Chem. 90 (12), 7708–7714.
Wang, X.D., Xie, Y., He, R., Zhang, J., Arman, H.D., Mohammed, O.F., Schanze, K.S., 2024. Inorg. Chem. 63, 11583–11591.

Wang, Z.Y., Dai, B.L., Su, Y.M., Hu, H.H., He, X.R., Chen, J.W., Wang, C., 2023. Inorg. Chem. 62, 11809–11816.
Wong, J.M., Zhang, R.Z., Xie, P.D., Yang, L.Q., Zhang, M.L., Zhou, R.X., Wang, R.Y., Shen, Y., Yang, B., Wang, H.B., Ding, Z.F., 2020. Angew. Chem. Int. Ed. 59, 17461–17466.
Wu, K.Q., Zheng, Y.J., Chen, R., Zhou, Z.X., Liu, S.Q., Shen, Y.F., Zhang, Y.J., 2023. Biosens. Bioelectron. 223, 115031.
Wu, P., Hou, X., Xu, J.J., Chen, H.Y., 2014. Chem. Rev. 114, 11027–11059.
Wu, S.J., Ren, D., Zhou, K., Xia, H.L., Liu, X.Y., Wang, X., Li, J., 2021. J. Am. Chem. Soc. 143, 10547–10552.
Xiao, H., Wang, Y., Zhao, Y., Zhang, R.F., Kang, K.N., Feng, Y.J., Gao, Y.L., Guo, H.X., Lu, B.Z., Du, P.Y., Lu, X.Q., 2024. Chem. Sci. 15, 16681–16687.
Xie, X.J., Lian, Y.W., Xiao, L.H., Wei, L., 2020. Spectrochim. Acta, Part A 240, 118594.
Yang, Y., Wang, J.M., Liang, W.B., Li, Y., Yuan, R., Xiao, D.R., 2024. Anal. Chem. 96, 16362–16369.
Zhang, W.Q., Li, Q.Y., Zhang, Q., Lu, Y., Lu, H., Wang, W., Zhao, X., Wang, X.J., 2016. Inorg. Chem. 55, 1005–1007.
Zhang, X.Y., Chen, X.Z., Zhang, Y.Y., Liu, K.Z., Shen, H.J., Zheng, E., Huang, X.Q., Hou, S.C., Ma, X.D., 2019. Anal. Bioanal. Chem. 411, 7957–7966.
Zhu, D., Zhang, Y., Bao, S.S., Wang, N.N., Yu, S.Q., Luo, R.G., Ma, J., Ju, H.X., Lei, J.P., 2021. J. Am. Chem. Soc. 143, 3049–3053.
Zhu, Z.T., Zeng, C.Q., Zhao, Y.Q., Ma, J.J., Yao, X.Q., Huo, S.H., Feng, Y.J., Wang, M., Lu, X.Q., 2023. Angew. Chem. Int. Ed. 62, e202312692.